PCCP

PAPER

Check for updates

^{57}Fe-Enrichment effect on the composition and performance of Fe-based O$_2$-reduction electrocatalysts†

Kathrin Ebner,[a] Lingmei Ni,[b] Viktoriia A. Saveleva,[a] Benjamin P. Le Monnier,[c] Adam H. Clark, [iD][a] Frank Krumeich, [iD][d] Maarten Nachtegaal,[a] Jeremy S. Luterbacher, [iD][c] Ulrike I. Kramm, [iD][b] Thomas J. Schmidt [iD][ae] and Juan Herranz [iD]*[a]

Pt-group metal (PGM)-free catalysts of the Me–N–C type based on abundant and inexpensive elements have gained importance in the field of oxygen reduction reaction (ORR) electrocatalysis due to their promising ORR-activities. Their insufficient stability, however, has fueled the interest in obtaining an in-depth understanding of their composition, which requires highly sensitive techniques compatible with their low metal contents (typically <5 wt%). In the particular context of iron-based materials, ^{57}Fe-Mössbauer spectroscopy is often used to provide such compositional information, but requires (partially) ^{57}Fe-enriched precursors. As a consequence, the extrapolation of conclusions drawn from Mössbauer measurements on ^{57}Fe-enriched catalysts to equivalent materials with the standard isotope distribution relies on the assumption that the metal precursor's isotopic profile does not affect the catalysts' composition and ORR-activity. To verify this hypothesis, in this study we prepared two series of Fe-based catalysts using distinctively different synthesis approaches and various relative contents of ^{57}Fe-enriched precursors, and observed that the extent of the latter parameter significantly affected the catalysts' ORR-activity. This effect was successfully correlated with the Fe-speciation of the catalysts inferred from the characterization of these samples with Mössbauer and X-ray absorption spectroscopies. Ultimately, these results highlight the crucial importance of verifying the consistency of the catalysts' activity and composition upon comparing standard and ^{57}Fe-enriched samples.

Introduction

Polymer electrolyte fuel cells (PEFCs) are energy conversion devices well-suited for automotive applications. The underlying reactions taking place at their cathode and anode are the reduction of oxygen and the oxidation of hydrogen, respectively, thus yielding water as a product in a process that can be

[a] *Paul Scherrer Institut, 5232 Villigen PSI, Switzerland. E-mail: juan.herranz@psi.ch*

[b] *TU Darmstadt, Department of Chemistry and Department of Materials- and Earth Sciences, Catalysts and Electrocatalysts Group, 64287 Darmstadt, Germany*

[c] *EPFL Lausanne, Laboratoire des Procédés Durables et Catalytiques, 1015 Lausanne, Switzerland*

[d] *ETH Zürich, Laboratory of Inorganic Chemistry, 8093 Zürich, Switzerland*

[e] *ETH Zürich, Laboratory of Physical Chemistry, 8093 Zürich, Switzerland*

† Electronic supplementary information (ESI) available: Detailed experimental information regarding the synthesis and materials characterization procedures; Mössbauer spectra, their deconvolution parameters and corresponding quantified results; Raman spectra, their deconvolution parameters and the corresponding D/G-band ratios; physicochemical properties (XPS, N$_2$-sorption and bulk Fe-content results); ORR-activity normalized by the catalysts' capacitance; XANES and EXAFS spectra and fits. See DOI: 10.1039/d1cp00707f

regarded free of carbon-based emissions as long as the hydrogen fuel is produced from renewable sources. Thus, PEFCs have tremendous potential to make a game-changing contribution to the urgently required decarbonization of the transportation sector, especially for vehicle segments needing large driving ranges (>500 km) and fast refueling times (<10 min).[1] Nevertheless, the large scale application of these devices is hindered by their high price, whereby ≈40% of the PEFC stack cost is projected to arise from the Pt-based catalysts typically employed in both PEFC electrodes (on the basis of a production volume of 500 000 FC vehicles per year).[2] Considering that the scarcity of this noble metal adds additional obstacles for upscaled production,[3] these shortcomings fuel the search for alternative catalysts, especially for the reduction of O$_2$, which requires Pt-loadings ≥5-fold larger than those for H$_2$-oxidation.[4–6]

With this motivation, and as a result of their promising catalytic activities and reliance on abundant materials, platinum group metal (PGM)-free catalysts of the Me–N–C type play an increasingly important role in the field of oxygen reduction reaction (ORR) electrocatalysis for PEFC applications.[7,8] However,

This journal is © the Owner Societies 2021

Phys. Chem. Chem. Phys., 2021, **23**, 9147–9157 | 9147

Paper

PCCP

the widespread commercialization of such materials is currently prevented by their relatively fast degradation upon operation, which has been linked to a large variety of deactivation mechanisms.[9–17] Some among these have related the performance loss to the speciation of the metal in the catalysts (Me, typically Fe, Co or Mn, as well as mixtures thereof). In the specific case of the better-studied, Fe-based materials, which currently feature the most promising ORR-activities,[18–22] two species are customarily observed by compositional analysis: (i) inorganic, Fe-based particles (*e.g.*, α-Fe, Fe_3C and/or Fe_xN)[23–27] formed during the high-temperature treatments involved in the catalysts' synthesis; and (ii) molecularly-dispersed sites in which an Fe-ion is coordinated by N-functionalities embedded in their carbon matrix.[24,28–31] While the latter, so-called Fe–N_x-moieties have additionally been proposed to be the ORR-active sites in these catalysts,[23–26,28,32–34] the former inorganic particles have been related to the materials' instability. Specifically, their progressive leaching can lead to ionomer-immobilized Fe-ions that decompose ORR-related H_2O_2 into aggressive radicals (*e.g.*, $OH^{\bullet-}$), which in terms corrode the carbon support and ionomer phase.[26] Aside from being paramount to the understanding of these degradation processes, insights into the detailed Fe-speciation of the materials, including geometry, oxidation and spin states of their Fe–N_x-sites, are crucial as these parameters are expected to determine their turn over frequencies (TOFs) towards the ORR.[35,36]

Due to its sensitivity towards the structural, chemical, magnetic and electronic nature of an atom's local environment, Mössbauer spectroscopy (MS) is a powerful tool allowing for the differentiation and quantification of the Fe-species in these and other heterogeneous materials. As a consequence, over the last decades this technique has been successfully used for understanding the structure of a variety of catalyst systems,[37] including these Fe-based, ORR-active materials.[24,27,38–41] To observe a detectable Mössbauer effect and obtain appropriate signal resolution, nuclear transitions with an appropriate energy and lifetime of the excited state are needed. In the case of iron, such requirements are fulfilled for ^{57}Fe,[42] but its natural abundance only amounts to 2.2% of all iron isotopes.[43] As a result, the characterization with MS of low Fe-content materials like these Fe-based O_2-reduction catalysts, which typically feature <5 wt% Fe, often requires the materials to be synthesized with ^{57}Fe-enriched precursors to keep reasonable measurement times and a high signal-to-noise ratio. Since these precursors are often cost-intensive, they are typically employed only when the resulting compound is to be studied with MS. Thus, while in an ideal case all characterization should be performed on the identical isotopically enriched catalyst, in practice compositional results inferred from MS measurements of ^{57}Fe-enriched samples are often compared to (electro-)catalytic and physicochemical features displayed by non-enriched analogues. Chiefly, the reliability of such comparison strongly relies on the assumption that those properties are not affected by the nature of the metal precursor, which to the best of our knowledge has never been systematically investigated in the existing literature.

With this motivation, herein we focus our attention on the influence of the extent of ^{57}Fe-enrichment in the precursor

mixture on the compositional properties and ORR-activity of Fe–N–C catalysts prepared using polyacrylonitrile (PAN) as the C- and N-source, Na_2CO_3 as the pore inducing agent and Fe(II)–acetate as the metal precursor. As a bulk probe, ^{57}Fe-sensitive MS measurements of the (partially) isotopically-enriched samples are complemented by X-ray absorption spectroscopy (XAS) results featuring a similar, but not isotope specific sensitivity to the Fe-speciation.[23,32] This data is further accompanied by a rotating disk electrode (RDE) voltammetric[44] analysis of the catalysts' electrochemical activity towards the ORR. Additionally, the activity and composition of a series of catalysts prepared by impregnation of iron(III)–porphyrin on carbon black (*vide infra*) were investigated in order to understand the applicability of our findings to such a "model" ORR-catalyst system.

Our results clearly demonstrate the strong influence of the degree of ^{57}Fe-enrichment on the catalysts' composition and ORR-activity for both of these catalyst systems. Specifically, for the materials synthesized using FeAc as a precursor, the results of these techniques unveil a direct qualitative correlation between the catalysts' ^{57}Fe-enrichment extent and their content of Fe-based inorganic side phases (*i.e.* carbide or metallic Fe), which in terms leads to a concomitant decrease in the concentration of molecularly dispersed, Fe–N_x-like sites and a lower ORR-activity. On the contrary, the porphyrin-based materials show increased ORR-activity for higher ^{57}Fe-enrichment extents, caused by an altered distribution of the MS doublets assigned to Fe–N_x-sites with vastly different activity.[24,27,33,45] Ultimately, without fully elucidating the origins of this effect, these results imply that in order to draw unambiguous conclusions about a catalytic system's composition and activity on the basis of MS results, it is of utmost importance to verify whether the catalysts' characteristics remain unaffected upon transitioning from a non-enriched to an ^{57}Fe-enriched material – a crucial conclusion that, to the best of our knowledge, has not yet been reported in the field.

Experimental methods

The following paragraphs aim to give a brief overview of the experimental methods employed in this work to thoroughly characterize the FeAc-based catalyst series. A more detailed description of all materials' preparation and characterization procedures is provided in the ESI.†

Material preparation

The FeAc-based catalysts were prepared according to a synthesis procedure presented in a previous publication.[46] Fe(II)–acetate was used as the Fe-precursor, while PAN and Na_2CO_3 serve as the C- and N-precursor and the pore inducing agent, respectively. The precursors underwent mixing and ballmilling and two heat treatment steps (first at 700 °C and subsequently at 950 °C) in a reductive atmosphere with an in-between acid washing step to remove soluble Fe-phases.

To produce the series of catalysts with varying extents of ^{57}Fe-enrichment, the ratio of ^{57}Fe-enriched and standard Fe-precursor

9148 | *Phys. Chem. Chem. Phys.*, 2021, **23**, 9147–9157

This journal is © the Owner Societies 2021

was varied to reach the desired ^{57}Fe-enrichment of each catalyst x_{cat} according to eqn (1):

$$x_{cat} = \frac{m(^{57}\text{Fe-prec.})}{m(\text{Fe-prec.}) + m(^{57}\text{Fe-prec.})} \times x_{^{57}\text{Fe-prec.}} + \frac{m(\text{Fe-prec.})}{m(\text{Fe-prec.}) + m(^{57}\text{Fe-prec.})} \times 0.022 \quad (1)$$

where $m(^{57}\text{Fe-prec.})$ and $m(\text{Fe-prec.})$ were defined as the weighed amounts (i.e., masses) of the ^{57}Fe-enriched and standard Fe-precursor, respectively, while $x_{^{57}\text{Fe-Prec.}}$ refers to the grade of ^{57}Fe-enrichment in the enriched precursor material as specified by the supplier (i.e., for FeAc, $x_{^{57}\text{Fe-Prec.}}$ = 95%). The factor 0.022 stems from the content of ^{57}Fe in the natural isotope mixture.[43]

Electrochemical testing

The materials' electrocatalytic activity towards the ORR was determined by the means of RDE voltammetry.[44] Catalyst inks were prepared from ultrapure water, isopropanol and Nafion ionomer dispersion and dropcasted on mirror-polished glassy carbon disks to yield a loading (m_{Cat}) of 500 $\mu g_{catalyst}$ cm^{-2}. ORR-polarization curves were acquired in O_2-saturated, 0.1 M HClO$_4$ electrolyte, while the capacitive current contribution was recorded in N_2-satured environment. The ORR-activity was determined at 0.8 V vs. RHE by calculating the ORR-specific faradaic current density (i_F, eqn (2)) and, based on that, the kinetic current density (i_{kin} in A g^{-1}) via eqn (3).

$$i_F = i - i_{cap} \quad (2)$$

$$i_{kin} = \frac{1}{m_{cat}} \times \frac{i_{lim} \times i_F}{i_{lim} - i_F} \quad (3)$$

where i is the current density measured in O_2-saturated electrolyte and i_{lim} is the diffusion-limited current density (determined from the plateau of i_F at 0.05 V vs. RHE).

Material characterization

To obtain information about the surface elemental composition of the materials, X-ray photoelectron spectra were recorded and energy calibrated (C1s peak at 284.6 eV), and the N1s peak was deconvoluted to obtain information on the pyridinic, nitrilic/Me–N$_x$-type, pyrrolic, graphitic and oxidized surface N-contents. The parameters applied for deconvolution can be found in ref. 47.

The Brunauer–Emmett–Teller (BET) equation was used in a relative pressure range from $0.02 \leq p/p_0 \leq 0.12$ to calculate the total surface area of selected catalysts from N_2-physisorption measurements.

The bulk Fe-contents were determined by measuring inductively coupled plasma optical emission spectroscopy (ICP-OES).

Scanning transmission electron microscopy (STEM) measurements were performed in an HD-2700CS microscope (Hitachi) or an FEI Talos F200X apparatus, obtaining bright field (BF) as well as (high-angle) annular dark field ((HA)ADF) images, while the morphology was studied with secondary electron detection. Energy-dispersive X-ray (EDX) spectroscopy was employed to gather information about the elemental composition in certain areas.

X-Ray absorption spectra were recorded at the SuperXAS beamline of the Swiss Light Source at the Fe K-edge in either fluorescence- or transmission-detected quick-scanning mode.[48,49] Data treatment was performed using the Demeter software package[50] and ProXAS[51] and included calibration, normalization, linear combination fitting (LCF) and multivariate curve resolution (MCF) of the XANES spectra as well as Fourier-transforming and fitting the EXAFS region.

Mössbauer spectroscopic measurements were carried out in transmission mode at room temperature. The obtained data was analyzed with the Recoil software and fitted using the components displayed in Table S1 (ESI†), assuming Lorentzian-shaped signals for all Fe-sites. The relative absorption areas of the different species were corrected by the respective Lamb–Mössbauer factors (LMF) as determined by Sougrati et al. in ref. 27 and listed in Table S2 (ESI†).

Raman spectra were acquired using a Raman microscope with a He–Ne excitation laser (632.8 nm). Every spectrum was the average of 15 acquisitions. The fitting of the Raman spectra was done by applying 4 Lorentzian profiles, whereby the constraints of band positions and widths are shown in Table S3 (ESI†).

Results and discussion

ORR-activity and physicochemical characterization of the FeAc-based catalysts

To verify that the compositional results reported below are not affected by inconsistencies in the oxidation state of the metal precursors used in the catalysts' synthesis, X-ray absorption spectra of the ^{57}Fe-enriched and standard Fe(II)–acetates used for the synthesis of all FeAc-based catalysts featured in this study were recorded (see Fig. S1, ESI†). Great care was taken in the samples' preparation and transportation to avoid any contact with oxygen and moisture (cf. Experimental section in the ESI†). Additionally, an aged sample exposed to the ambient atmosphere for several weeks was measured for comparison. The XANES spectra of the two ferrous salts are almost identical and their features also match what was reported for Fe(II)–acetate,[52] thus confirming the integrity of these starting materials. The aged sample, on the other hand, displays a significant shift of the absorption edge that indicates a change of oxidation state and highlights the importance of appropriate storage of this Fe(II) salt. It is for this reason that, throughout all syntheses and analyses, these precursors were kept inside an air- and moisture-free Ar-filled glovebox in order to preserve this initial state (see the Experimental section in the ESI† for details).

Following this verification, a series of four catalysts with an equal, initial Fe-content of 0.5 wt% Fe (on the basis of all precursors' masses) but different extents of ^{57}Fe-enrichment were prepared and tested electrochemically using RDE voltammetry (see representative polarization curves in Fig. S2, ESI†).[44] As displayed in Fig. 1a, these materials featured a systematic, up to $\approx$4-fold decrease of their ORR-activity with increasing ^{57}Fe-content. Chiefly, this trend cannot be related to differences

This journal is © the Owner Societies 2021

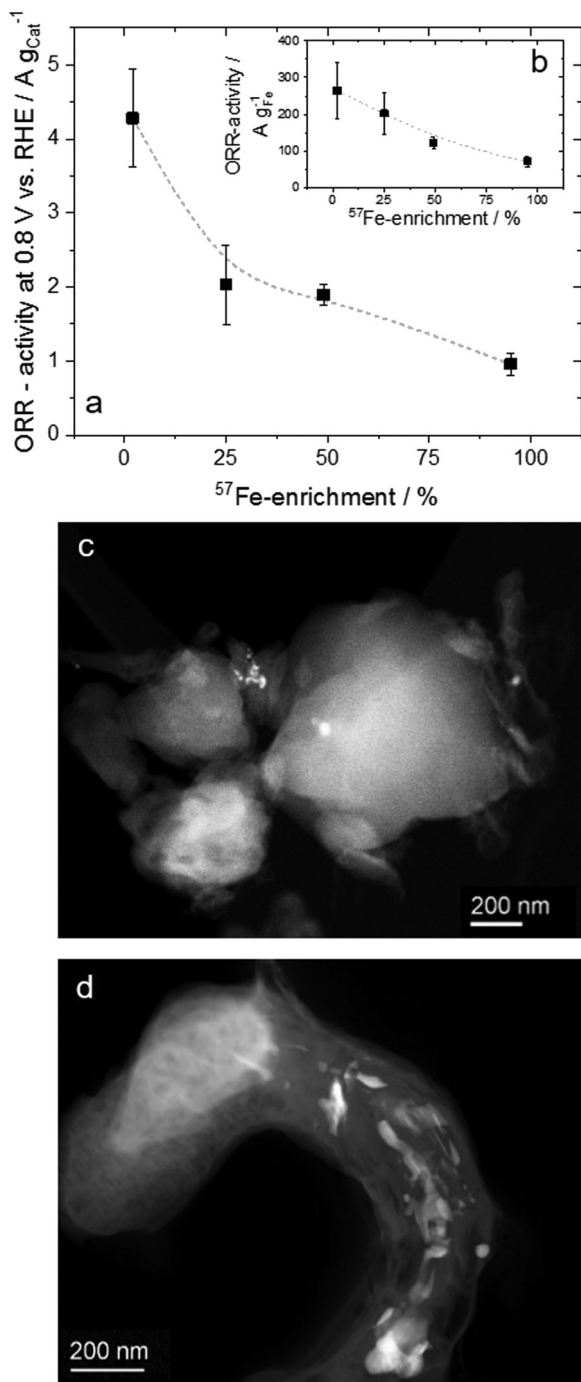Phys. Chem. Chem. Phys., 2021, **23**, 9147–9157 | **9149**

Fig. 1 Effect of the degree of ^{57}Fe-enrichment of four FeAc-based catalysts on their electrochemical activity towards the ORR, expressed as the kinetic current at an iR-corrected potential of 0.8 V vs. RHE and normalized with regard to the catalysts' overall mass (a) or by their final Fe-content (b). Dashed lines are mere guides to the eye. STEM images of a non- (c) and a fully ^{57}Fe-enriched material (d), whereby the technique's Z-contrast reveals the presence of a proportionally greater amount of Fe-based side phases (corresponding to the brighter spots) in the ^{57}Fe-enriched sample.

in the catalysts' overall Fe-concentration or electrochemical double layer capacitance, which remain comparable for all four samples (at ≈ 1.0–1.5 wt% Fe and ≈ 260–300 F g^{-1}, respectively – cf.

Fig. S3a and b, ESI†), and remains valid when their ORR-activity is normalized with respect to these parameters (see Fig. 1b and Fig. S4, ESI†). Further, neither the surface area determined from N$_2$-sorption nor the relative contents of pyridinic-, pyrrolic- and Me–N$_x$-type surface nitrogen functionalities that have been related to the coordination of the iron ions in the ORR-active Fe–N$_x$-sites show systematic differences (see Fig. S3c and d, along with the deconvoluted XPS spectra in Fig. S5, ESI†), and can therefore also be excluded as the main cause for the observed ORR-activity differences.

Fe-speciation of the FeAc-based catalysts

In order to identify the origin of this systematic ORR-activity change, the fully enriched ($>95\%$ ^{57}Fe) and non-enriched (2% ^{57}Fe, natural abundance) samples were consequently studied with STEM. The technique's Z-contrast allows for an unambiguous detection of Fe-based inorganic particles that could be formed during the synthesis' pyrolysis step(s).[25,26,46] While the contribution of such particles to the catalysts' overall ORR-activity remains a subject of vivid debate,[18,24,29–31,53–56] their likely detrimental impact on their degradation[26] implies that a high amount of such inorganic species in the material can be an indicator of poor stability. As demonstrated in Fig. 1d, a significant amount of these particles, which are indeed Fe-based as verified by EDX, were spotted in the fully ^{57}Fe-enriched material. This is in contrast to the catalyst synthesized using the standard, non-^{57}Fe-enriched metal precursor, in which only a minor amount of particles could be found upon inspection (cf. Fig. 1c). This observation is even more pronounced for an equivalent series of catalysts produced with a lower initial Fe-content of 0.1 wt% Fe; whereas no particles could be found in the non-enriched material even when using a large magnification (cf. Fig. S6a, ESI†), numerous Fe-based particles were present in an equivalent catalyst prepared with a 95% ^{57}Fe-enrichment extent (see Fig. S6b, ESI†). Most importantly, these catalysts with an initial Fe-content of 0.1 wt% Fe are also affected by the concomitant decrease of the ORR-activity with the ^{57}Fe-concentration observed for the 0.5 wt% Fe series discussed so far (cf. Fig. S6c, ESI†). Note that these Fe-based particles are typically encapsulated in a ≥ 5 nm thick carbon shell[46] and are therefore unlikely to significantly contribute to the ORR-activity of the FeAc-based catalysts presented herein.[57]

A further, indirect indicator of the presence of an increasing amount of Fe-based inorganic particles in the catalysts with higher ^{57}Fe-enrichment extents are the differences in the structural properties of their carbonaceous matrix. These can be derived from Raman spectroscopy measurements (see Fig. S7a–d for the deconvoluted spectra, ESI†). Specifically, the ratio between the area of the D- and G-bands (cf. Fig. S7e, and the assignments in Table S3, ESI†) in the deconvoluted Raman spectra decreases by $\approx 25\%$ as the catalysts' ^{57}Fe-enrichment increases. Considering that this D/G-quotient is inversely proportional to the graphitization extent of the corresponding carbon,[58–62] this trend is consistent with the increasing presence of Fe-based particles in the ^{57}Fe-enriched catalysts, since such metallic particles are known to catalyze C-graphitization.[63–65]

Even though STEM and Raman measurements provide valuable preliminary insight into these compositional differences, the derived results are exclusively qualitative (or, in the case of Raman spectroscopy, only indirectly related to the catalysts' Fe-speciation – *vide supra*). Thus, to obtain more precise information about the catalysts' bulk Fe-composition, we performed the MS measurements for which ^{57}Fe-enrichment is customarily intended. This technique allows a quantitative deconvolution of the different species in these Fe-based catalysts thanks to its sensitivity to their chemical and magnetic environments. It should be emphasized at this point that the technique only probes the ^{57}Fe-nucleii present in an analyte, and thus its quantitative nature is based on the assumption that all Fe-atoms behave like this detectable ^{57}Fe-isotope – a key assumption that we are aiming to verify in this study.

With this consideration in mind, the deconvoluted Mössbauer spectra of the three ^{57}Fe-enriched catalysts appear plotted in Fig. 2, and Table S1 (ESI†) displays the fitting parameters of the various Fe species found in the materials. Specifically, these consist of (i) three doublets previously assigned to Fe–N$_x$-sites with the iron ions in a ferrous form but different spin states,[24] and (ii) three sorts of inorganic iron agglomerate phases (superparamagnetic iron, α-Fe and Fe$_x$C) related to the spectra's singlet and two sextets. The distinct differences in these species' relative contributions appear quantified in Fig. 3a and b. Specifically, the solid lines display the sum of the relative absorption areas corresponding to the three doublets assigned to Fe–N$_x$-sites *vs.* the singlet and sextets related to inorganic Fe-based phases after correction by the respective Lamb–Mössbauer factors determined by Sougrati *et al.*[27] (see Table S2, ESI†). Complementarily, the individual, LMF-corrected relative absorption areas of each kind of Fe–N$_x$ site and inorganic iron phase are displayed in Fig. S8 (ESI†). These room temperature spectral results unambiguously demonstrate that higher extents of ^{57}Fe-enrichment lead to a pronounced increase in the presence of Fe-based particles (*i.e.*, from ≈40 to ≈60% of the LMF-corrected absorption area) accompanied by a concomitant decrease of the Fe–N$_x$-sites' content (*i.e.*, from ≈60 to ≈40%). We note in passing that the results plotted in Fig. 3a represent a simplified picture in which all three doublets have been assigned to Fe–N$_x$-sites, even if one of them (D1) has recently been shown to also contain contributions from inorganic side phases that can only be resolved through low temperature MS measurements at 4–5 K.[27,66]

Complementary to these MS results, *ex situ* XAS measurements of all four catalysts with varying degrees of ^{57}Fe-enrichment were performed. Fig. 4a displays their XANES spectra, which feature a systematic decrease of the white line as well as an enhancement of the pre-edge feature at ≈7114 eV upon increasing the ^{57}Fe-content. These differences can be explained based on the qualitative comparison between these spectra and that of Fe$_3$C (retrieved from ref. 67), which was determined to constitute the primary Fe-based inorganic phase in these materials in the above MS measurements (*cf.* Fig. S8, ESI†). As shown in Fig. S9 (ESI†), such a spectral juxtaposition confirms that higher extents of ^{57}Fe-enrichment lead to a greater resemblance with the iron carbide spectrum and relative content
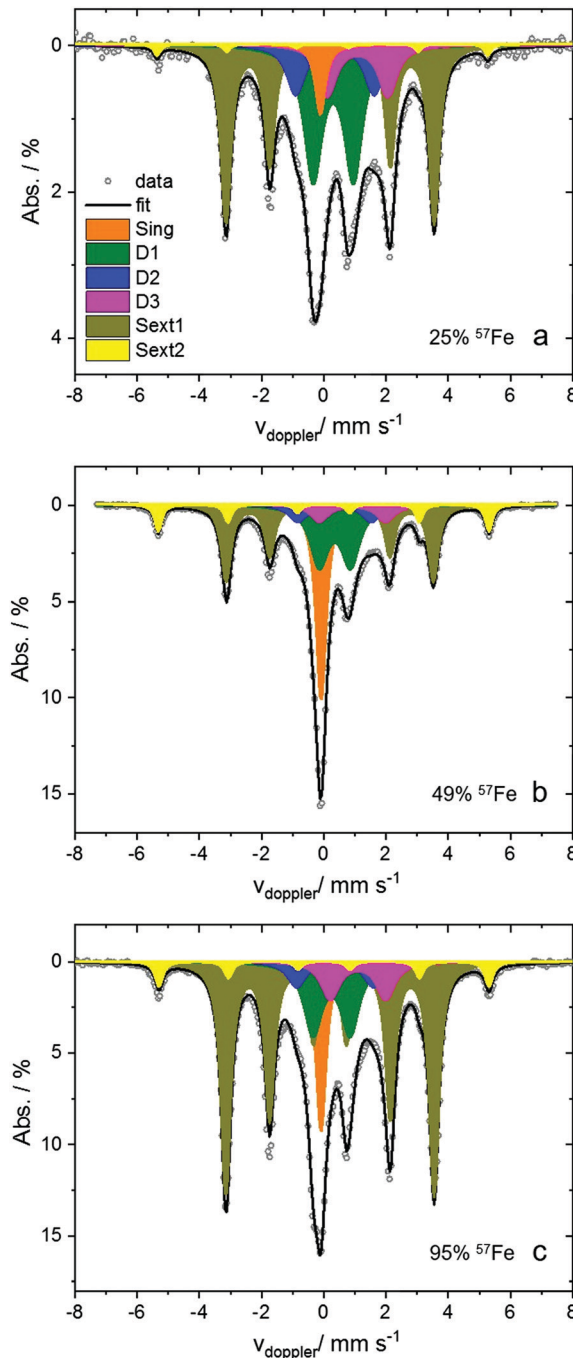

Fig. 2 Deconvoluted Mössbauer spectra of the samples synthesized with 25 (a), 49 (b) or 95% ^{57}Fe-enrichment (c), whereby the S1 singlet has been previously assigned to superparamagnetic iron, sextets 1 and 2 to iron carbide and α-Fe, and doublets 1, 2 and 3 to Fe–N$_x$-sites with iron in a 2+ oxidation state and a low, intermediate or high spin state, respectively (see Table S1 for a summary of the deconvolution results, ESI†).[24]

thereof. Complementarily, as the catalysts' ^{57}Fe-content decreases, their spectra increasingly resemble that of a catalyst preponderantly featuring Fe–N$_x$-like, molecularly dispersed sites (*i.e.*, the catalyst referred to as 'Fe0.5' in ref. 23) (see Fig. S9, ESI†). In an effort to quantify these differences, we proceeded to fit the XANES data with a linear combination fit (LCF) approach based on the
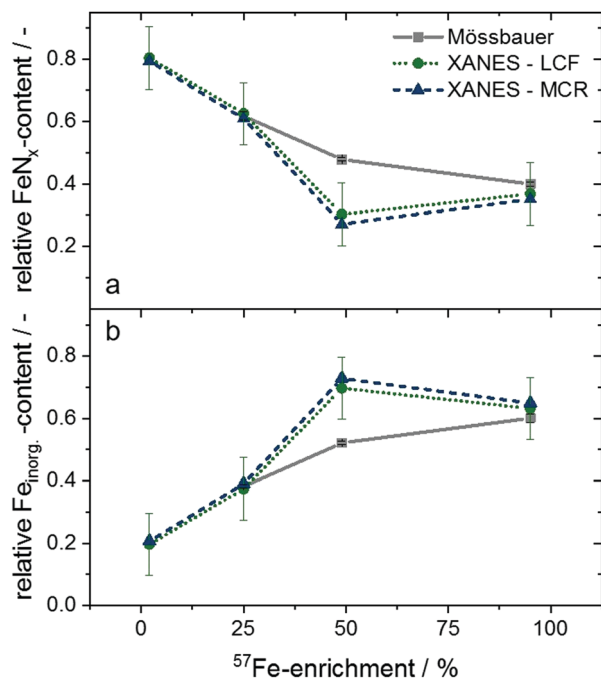
This journal is © the Owner Societies 2021

Phys. Chem. Chem. Phys., 2021, **23**, 9147–9157 | 9151

Fig. 3 Relative contents of Fe–N$_x$-sites (a) and inorganic particles (b) in the four catalysts with different extents of ^{57}Fe-enrichment, as derived from Mössbauer analysis (corrected for Lamb–Mössbauer factors, and only applicable to the three ^{57}Fe-containing samples) as well as LCF or MCR analysis of the corresponding XANES spectra in Fig. 4a. An error of ± 10% has been assumed for the LCF results and is indicated in the graph.

Fig. 4 XANES spectra of the four FeAc-based catalysts with different degrees of ^{57}Fe-enrichment, alongside the two spectral components derived from the MCR analysis (a), which are subsequently compared to the reference spectra of Fe–N$_x$-sites and Fe$_3$C employed for linear combination fitting (b). Note that the spectrum of the Fe–N$_x$-sites corresponds to that of the Fe0.5 sample in ref. 23.

two reference spectra of Fe$_3$C and Fe–N$_x$-sites discussed above (see Fig. S10 for all spectra and their corresponding LCFs, ESI†). As visualized in Fig. 3b (dotted line), the contribution of the Fe$_3$C component to the overall spectra grows indeed with rising ^{57}Fe-enrichment extents, while that of the Fe–N$_x$-sites (Fig. 3a, dotted line) declines from ≈ 80 to ≈ 40% when comparing a standard sample to a fully ^{57}Fe-enriched one. It should be kept in mind, though, that the fitting weight of the components only provides a rough estimate of the amount of Fe in the different species (that is, in inorganic particles vs. Fe–N$_x$-sites), since a more precise fit would require reference spectra for all different Fe-sites possibly present in these materials. Specifically for the Fe–N$_x$ molecular sites with different configurations and spin states,[24,68] these ideal references are, however, not available, since to the best of our knowledge no catalysts containing only one single type of such Fe–N$_x$-sites with homogeneous electronic and geometric properties have been reported in the existing literature. Furthermore, while Fe$_3$C is the most prominent side phase (as determined by MS, cf. Fig. S8 (ESI†) and the discussion above), other Fe-based inorganic species such as superparamagnetic and α-Fe are present in the material, thus adding uncertainty to the results derived from such a two-component fit.

In an effort to implement an alternative method of XANES analysis, we employed multivariate curve resolution (MCR), whereby the component differentiation problem is solved by breaking the raw data matrix down into component spectra and corresponding contributions applying asymmetric least squares
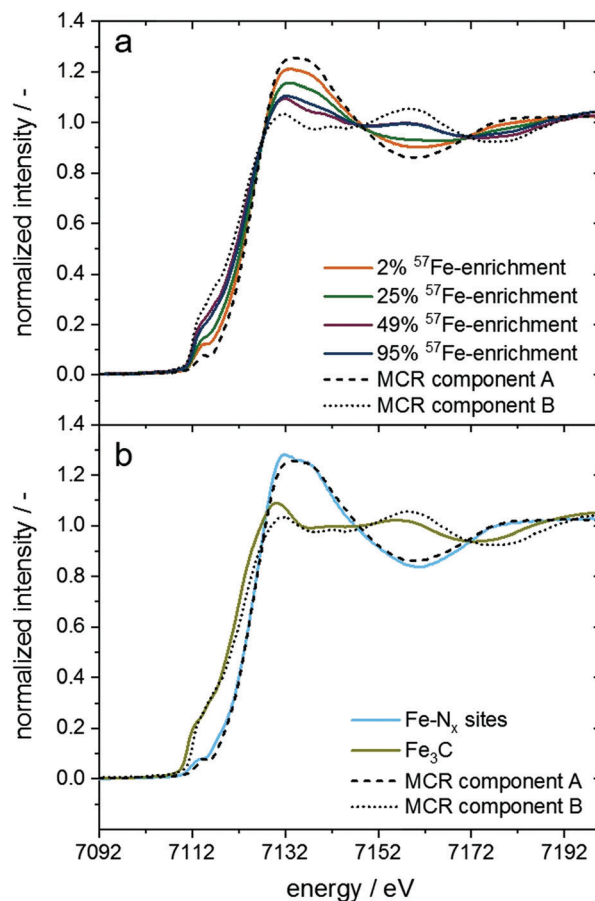
criteria. Details on this method can be found elsewhere.[69–71] The two components extracted from the analysis are shown in Fig. 4a alongside the XANES spectra of the materials and will be referred to as components A and B in the following. We note in passing that each of these components does not necessarily represent only a single Fe-speciation.[71] Interestingly, there are distinct differences in the shape of the spectra of the Fe$_3$C reference and component B drawn from the multivariate analysis (cf. Fig. 4b); specifically, the oscillations in the spectrum of Fe$_3$C have a higher frequency than the ones of component B, possibly because the latter displays a smaller lattice parameter than Fe$_3$C, indicating that the Fe-based inorganic particles in the catalyst have an average C/Fe-ratio smaller than that of stoichiometric Fe$_3$C. This agrees well with the results inferred from MS, where α-Fe and superparamagnetic iron were found to be present alongside this Fe$_3$C.

At the same time, the MCR-derived spectra for component A and that of the catalyst featuring a majority of Fe–N$_x$-sites[23] bear a strong resemblance, further confirming that Fe–N$_x$-moieties are indeed present in these materials. Most importantly, despite these differences in the spectral features of reference samples vs. MCR-inferred

9152 | Phys. Chem. Chem. Phys., 2021, 23, 9147–9157

This journal is © the Owner Societies 2021

compounds, the proportions of these two components in the catalysts with different degrees of [57]Fe-enrichment drawn from the MCR analysis are roughly the same (if with comparatively smaller fitting residuals) as those derived for the Fe–N$_x$-sites and Fe$_3$C using the above linear combination approach (see dashed vs. dotted lines, respectively, in Fig. 3a and b).

Similar qualitative trends in composition can be found upon inspection of the Fourier-transformed EXAFS spectra displayed in Fig. 5a, for which higher [57]Fe-contents result in an intensification of the Fe–Fe scattering peak at ≈ 2.2 Å[23] (without phase shift corrections) and a drop of the Fe–O/N/C scattering peak at ≈ 1.5 Å attributed to Fe–N$_x$-sites.[23,46] This behavior is well reflected in the structural parameters derived from the best fits of the first scattering shell listed in Table S4 (please refer to Fig. S11 for a visualization of the actual fits, ESI†). The corresponding changes in the coordination numbers as a function of the catalysts' [57]Fe-enrichment extent are additionally displayed in Fig. 5b. The significant increase of the Fe–Fe coordination number with [57]Fe-enrichment can be explained by assuming that an increasing number of iron atoms are present in the Fe-based inorganic particles' domains, which therefore become larger as the enrichment extent increases. At the same time, the coordination number of the Fe–O/N/C scatterer progressively decreases from ≈ 4.5 to ≈ 3.5 (i.e., by $\approx 22\%$) upon increasing the

[57]Fe-enrichment from 2 to 95%, but this drop is not as strong as the $\approx 55\%$ relative decrease of the Fe–N$_x$-sites content inferred from the LCF and MCR analyses (see Fig. 3a). This is caused by the carbide particles' Fe–C scattering contribution, which overlaps with the other light elements' (i.e., O, N) scattering paths and increases with the [57]Fe-enrichment extent and corresponding concentration of inorganic Fe-particles (vide supra). On the other hand, we refrain from fitting the second coordination shell (>3 Å, non-phase corrected) due to the limited data range available (cf. k-space of the spectra displayed in Fig. S12, ESI†).

Generally speaking, the compositional results derived from the two bulk techniques employed herein (namely, MS and XAS) are in good qualitative agreement among each other: increasing the degree of [57]Fe-enrichment causes a distinct decrease of the Fe–N$_x$-sites' content that is accompanied by a significantly enhanced presence of Fe-based inorganic particles (cf. Fig. 3), for which the relative concentration increases ≈ 3-fold upon raising the [57]Fe-enrichment from 2 to 95%. Looking at the differences among quantitative results, though, a disagreement among XAS- and MS-derived compositions can be observed in the specific (and unique) case of the 49% [57]Fe-enriched sample, for which XAS- vs. Mössbauer spectroscopy-derived Fe–N$_x$-sites contents account for ≈ 30 vs. $\approx 50\%$, respectively (see Fig. 3a). This punctual inconsistency could potentially be explained by a heterogeneous distribution of the inorganic Fe-based particles throughout the sample, especially considering that MS probes the bulk average of roughly 100 mg of catalyst, while with XAS only a comparatively smaller sample amount (<1 mg) was examined. Beyond this inconsistency, the otherwise excellent agreement among the compositions derived from XAS and MS have important implications for the application of the latter technique to the characterization of partially [57]Fe-enriched catalysts. More precisely, the good match among the isotopically sensitive [57]Fe MS results and those drawn from XAS, unaffected by the type of isotope, seems to confirm that for a material featuring mixtures of standard Fe and [57]Fe the isotopes are identically distributed among inorganic particles and Fe–N$_x$-sites, at least within the certainty allowed by the experimental error margins of both techniques. Most importantly, this also implies that the results derived from [57]Fe-sensitive MS of such isotopically mixed samples are representative of their overall Fe-speciation.

Interestingly, we have also observed an effect of the [57]Fe-enrichment extent on the ORR-activity for a substantially different type of Fe–N–C catalyst prepared by impregnating Fe(III)–porphyrin FeTMPPCl on carbon black and subsequent heat treatment (see Experimental section for details). In this synthesis approach, the Fe-precursor is implemented in the form of a well-defined, macrocyclic Fe–N$_4$-coordination environment provided by the porphyrinic precursor; this is in contrast to the FeAc-based preparation method, in which the iron is coordinated by six N-groups from the phenanthroline ligands in the precursor complex. As discussed in the Supplementary Information (see the 'Activity and composition of porphyrin-based catalysts' section, along with Fig. S13–S19, ESI†), modifying the degree of [57]Fe-enrichment between 2 and 98% led to a significant increase of activity accompanied by less pronounced alterations of
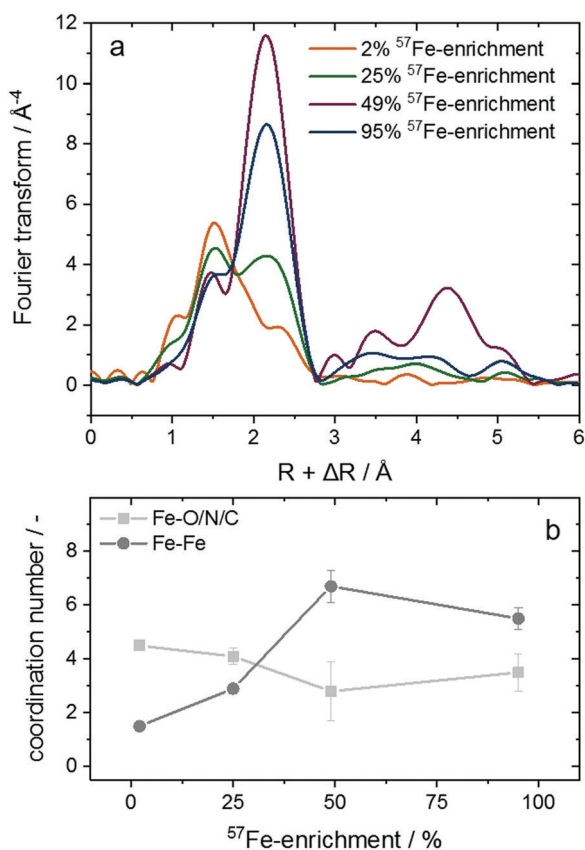

Fig. 5 Fourier-transformed EXAFS spectra of the four FeAc-based catalysts with different degrees of [57]Fe-enrichment (a), and the corresponding coordination numbers for Fe–O/N/C vs. Fe-Fe scatterers derived from the best fits of the EXAFS data in an R-range of 1–3 Å (b).

This journal is © the Owner Societies 2021

Phys. Chem. Chem. Phys., 2021, 23, 9147–9157 | 9153

the composition characterized by Mössbauer spectroscopy. Specifically, the LMF-corrected, relative absorption area of the D1 doublet increases with ^{57}Fe-enrichment, leading to a decline of the relative contribution of other Fe–N$_x$ signatures. At the same time, superparamagnetic iron is the only inorganic phase present in this set of catalysts and represents a minority species ($<10\%$) whose content slightly rises when increasing the ^{57}Fe-enrichment from 2 to 98%.

Relating ORR-activity and catalyst composition

Following this careful assessment of the catalysts' composition, we finalize this study by revisiting the effect of this variable on the materials' ORR-activity, displayed in Fig. 1a and Fig. S13 (ESI†) (for the FeAc- vs. the porphyrin-based samples, respectively). Notably, a quantitative relation between the absolute Fe-content in the form of a given MS site assigned to atomically dispersed Fe–N$_x$-sites (i.e. D1, D2, D2*, D3 or D4) and the activity applicable to all catalysts could not be established, as illustrated by the absence of linear relations between these variables displayed in Fig. S20 (ESI†). This lack of activity–composition–relation should not come as a surprise when comparing catalysts resulting from two different synthesis strategies, since properties other than their Fe-speciation could have a potential influence on their ORR-activity. Examples suggested by other authors include the micro- and mesoporous content and the surface N-speciation and -concentration,[31,47,72,73] but further descriptors are also likely to affect this trend.

We then continue by assessing a possible composition–activity–relation for each individual set of catalysts. For the FeAc-based materials, the ORR-activity decreases with growing degree of ^{57}Fe-enrichment – an effect that seems to go hand in hand with the pronounced decrease of the content of atomically dispersed Fe–N$_x$-sites determined by XAS and MS (cf. Fig. 4a). Specifically, the content of such atomically-dispersed centers determined by XANES analysis drops from ≈ 80 to $\approx 37\%$ when comparing the none- and the fully ^{57}Fe-enriched samples. MS deconvolution confirms that the majority of these Fe–N$_x$-sites losses come from the D2 and the D1 sites (cf. Fig. S8, ESI†), whereby the latter is widely agreed to significantly contribute to the catalysts' activity.[24,33,74–76] Nevertheless, the $\approx 50\%$ decrease in the relative content of these D1 sites (see Fig. S8, ESI†) combined with the minor differences among the catalysts' Fe-contents (cf. Fig. S2a, ESI†) cannot fully justify the ≈ 3-fold loss of Fe-content normalized ORR-activity observed for these catalysts (cf. Fig. 1b). Analogously, in the case of the porphyrin-based system, an increase of the ^{57}Fe-enrichment leads to a greater share of D1 out of the total LMF-corrected relative absorption area assigned to Fe–N$_x$-sites (cf. Fig. S21, ESI†); however, the 20% increase in these D1 sites that have been previously ascribed to the active sites in these catalysts[24,74–76] does not fully explain the ≈ 3-fold ORR-activity gain observed with higher enrichment (cf. Fig. S13, ESI†). These inconsistencies in both catalyst systems could be related to and effect of the degree of ^{57}Fe-enrichment on the turn-over frequency of the ORR-active Fe–N$_x$-sites. However, they could also (partially) stem

from catalyst-specific differences in the fraction of these Fe–N$_x$-sites in contact with the electrolyte, and thus capable of participating in the ORR-process. Unfortunately, an accurate quantification of this number of active sites at the catalyst–electrolyte interface (i.e., utilization) is hindered by the lack of reliable in situ electrochemical probes for this determination.[77]

Lastly, we address potential origins of the observed performance and compositional changes affecting both catalyst series upon varying the extent of ^{57}Fe-enrichment. First of all, these effects are unlikely to result from discrepancies in the composition of the two metal precursors related to the iron itself, as supported by the matching XANES spectra displayed by the standard and ^{57}Fe-precursors used in the FeAc-based synthesis (see discussion above and Fig. S1, ESI†). Additionally, the ^{57}Fe- and standard Fe-variants of the porphyrin– and Fe–acetate-derived, phenanthroline complex display very similar thermal decomposition profiles (see Fig. S22, ESI†) that discard a difference in loss of these compounds' coordination environments during their heat treatment as the cause for the catalysts' dissimilar Fe-speciations and ORR-activities. Instead, we hypothesize that the observed differences in these properties stem from an isotope effect and/or from undetermined discrepancies in the impurity levels of the ^{57}Fe- vs. standard Fe-precursors. Unfortunately, the latter possibility is particularly hard to verify, since the purification and/or analysis of isotopically enriched salts would require relatively large amounts of these compounds that are incompatible with the small batch sizes in which these are generally prepared (in terms caused due to their high price).

Conclusions

In summary, in this study we applied several distinct methods to analyze the composition of two series of Fe–N–C catalysts that had been synthesized with Fe–acetate or an Fe–porphyrin (FeTMPPCl) as the iron source, and for which the degree of ^{57}Fe-enrichment had been varied between 2 and 98%. This last aspect is of great relevance, since ^{57}Fe-enriched mimics of iron-based PGM-free catalysts are often synthesized for the purpose of studying their composition with Mössbauer spectroscopy – a technique that is only sensitive to the ^{57}Fe isotope.

Our results revealed a strong influence of the share of ^{57}Fe-enriched material in the iron precursor on the resulting catalysts' composition, i.e., their corresponding contents of Fe-based inorganic particles and Fe–N$_x$-type sites. For the FeAc-based catalysts, the compositional trend inferred from XAS measurements was in good agreement with the results of MS, indicating that the observed effect of the ^{57}Fe-enrichment extent on the catalysts' composition does not stem from intrinsic differences in the isotopes' properties that may affect their distribution among the catalysts' various Fe-species.

While the ≈ 4-fold decline of the ORR-activity of the FeAc-based materials with a higher ^{57}Fe-enrichment extent could be qualitatively explained by the concomitant decrease of the Fe–N$_x$-sites' content, the three porphyrin-based samples displayed the opposite ^{57}Fe-enrichment vs. ORR-activity trend. Specifically,

9154 | Phys. Chem. Chem. Phys., 2021, **23**, 9147–9157

This journal is © the Owner Societies 2021

these samples' ORR-activity more than tripled upon increasing the [57]Fe-enrichment from 2 to 98%, even if in this case the concomitant compositional changes were not as drastic as for the FeAc-based series.

Even if the clarification of the origins of the observed compositional and performance changes are beyond the scope of this paper, the shown occurrence of an effect related to the fraction of [57]Fe-enriched precursors used in two kinds of catalysts produced through entirely different synthesis strategies strongly suggests that this is likely to happen to a certain extent in other Fe–N–C systems. Therefore, our results underline the importance of verifying the composition and performance of [57]Fe-enriched materials and their non-enriched counterparts in those cases in which physicochemical characterization and catalytic activity measurement are conducted on both [57]Fe-enriched and non-enriched catalysts. Clarifying these differences between non-enriched and enriched samples is particularly relevant when considering that the catalysts of choice for ultimate PEFC-implementation will feature the natural isotopic abundance.

Abbreviations

PGM	Pt-group metal
ORR	Oxygen reduction reaction
PEFC	Polymer electrolyte fuel cells
TOF	Turn-over frequency
MS	Mössbauer spectroscopy
XAS	X-Ray absorption spectroscopy
PAN	Polyacrylonitrile
DMF	Dimethylformamide
FeTMPPCl	5,10,15,20-Tetrakis(4-methoxyphenyl)-21H,23H-porphine iron(III) chloride
THF	Tetrahydrofuran
RDE	Rotating disk electrode
PTFE	Polytetrafluoroethylene
RHE	Reversible hydrogen electrode
CV	Cyclic voltammogramm
XPS	X-Ray photoelectron spectroscopy
BET	Brunauer–Emmett–Teller
ICP-OES	Inductively coupled plasma optical emission spectroscopy
NAA	Neutron activation analysis
STEM	Scanning transmission microscopy
EDX	Energy dispersive X-ray spectroscopy
LCF	Linear combination fit
SLS	Swiss Light Source
XANES	X-Ray absorption near edge structure
MCR	Multivariate curve resolution
EXAFS	Extended X-ray absorption fine structure
FT	Fourier-transformed
TCD	Thermal conductivity detector
TPD	Temperature programmed desorption
LMF	Lamb-Mössbauer factor

Author contributions

Conflicts of interest

There are no conflicts to declare.

Acknowledgements

Notes and references

1 O. Gröger, H. A. Gasteiger and J.-P. Suchsland, *J. Electrochem. Soc.*, 2015, **162**, A2605–A2622.

2 S. T. Thompson, B. D. James, J. M. Huya-Kouadio, C. Houchins, D. A. DeSantis, R. Ahluwalia, A. R. Wilson, G. Kleen and D. Papageorgopoulos, *J. Power Sources*, 2018, **399**, 304–313.

3 P. C. K. Vesborg and T. F. Jaramillo, *RSC Adv.*, 2012, **2**, 7933–7947.

4 K. C. Neyerlin, W. Gu, J. Jorne and H. A. Gasteiger, *J. Electrochem. Soc.*, 2007, **154**, B631.

5 K. C. Neyerlin, W. Gu, J. Jorne and H. A. Gasteiger, *J. Electrochem. Soc.*, 2006, **153**, A1955.

6 A. Rabis, P. Rodriguez and T. J. Schmidt, *ACS Catal.*, 2012, **2**, 864–890.

7 M. Shao, Q. Chang, J.-P. Dodelet and R. Chenitz, *Chem. Rev.*, 2016, **116**, 3594–3657.

8 F. Jaouen, D. Jones, N. Coutard, V. Artero, P. Strasser and A. Kucernak, *Johnson Matthey Technol. Rev.*, 2018, **62**, 231–255.

9 D. Banham, S. Ye, K. Pei, J. Ozaki, T. Kishimoto and Y. Imashiro, *J. Power Sources*, 2015, **285**, 334–348.

This journal is © the Owner Societies 2021

Phys. Chem. Chem. Phys., 2021, **23**, 9147–9157 | **9155**

10 C. H. Choi, C. Baldizzone, J. P. Grote, A. K. Schuppert, F. Jaouen and K. J. J. Mayrhofer, *Angew. Chem.*, 2015, **127**, 12944–12948.

11 J. Y. Choi, L. Yang, T. Kishimoto, X. Fu, S. Ye, Z. Chen and D. Banham, *Energy Environ. Sci.*, 2017, **10**, 296–305.

12 F. Jaouen, in *Non-Noble Metal Fuel Cell Catalysts*, ed. Z. Chen, J. Dodelet and J. Zhang, Wiley-VCH Verlag GmbH & Co. KGaA, Weinheim, 2014, pp. 29–118.

13 V. Goellner, C. Baldizzone, A. Schuppert, M. T. Sougrati, K. Mayrhofer and F. Jaouen, *Phys. Chem. Chem. Phys.*, 2014, **16**, 18454–18462.

14 V. Goellner, V. Armel, A. Zitolo, E. Fonda and F. Jaouen, *J. Electrochem. Soc.*, 2015, **162**, H403.

15 X. Yin and P. Zelenay, *ECS Trans.*, 2018, **85**, 1239–1250.

16 Y. Shao, J. P. Dodelet, G. Wu and P. Zelenay, *Adv. Mater.*, 2019, **31**(31), 1807615.

17 U. Martinez, S. Komini Babu, E. F. Holby and P. Zelenay, *Curr. Opin. Electrochem.*, 2018, **9**, 224–232.

18 K. Strickland, E. Miner, Q. Jia, U. Tylus, N. Ramaswamy, W. Liang, M. Sougrati, F. Jaouen and S. Mukerjee, *Nat. Commun.*, 2015, **6**, 7343–7349.

19 E. Proietti, F. Jaouen, M. Lefevre, N. Larouche, J. Tian, J. Herranz and J.-P. Dodelet, *Nat. Commun.*, 2011, **2**, 416.

20 J. Shui, C. Chen, L. Grabstanowicz, D. Zhao and D.-J. Liu, *Proc. Natl. Acad. Sci. U. S. A.*, 2015, **112**, 10629–10634.

21 X. Wan, X. Liu, Y. Li, R. Yu, L. Zheng, W. Yan, H. Wang, M. Xu and J. Shui, *Nat. Catal.*, 2019, **2**, 259–268.

22 A. Serov, K. Artyushkova, E. Niangar, C. Wang, N. Dale, F. Jaouen, M. T. Sougrati, Q. Jia, S. Mukerjee and P. Atanassov, *Nano Energy*, 2015, **16**, 293–300.

23 A. Zitolo, V. Goellner, V. Armel, M.-T. Sougrati, T. Mineva, L. Stievano, E. Fonda and F. Jaouen, *Nat. Mater.*, 2015, **14**, 937–942.

24 U. I. Kramm, J. Herranz, N. Larouche, T. M. Arruda, M. Lefèvre, F. Jaouen, P. Bogdanoff, S. Fiechter, I. Abs-Wurmbach, S. Mukerjee and J.-P. Dodelet, *Phys. Chem. Chem. Phys.*, 2012, **14**, 11673–11688.

25 U. I. Kramm, I. Herrmann-Geppert, S. Fiechter, G. Zehl, I. Zizak, I. Dorbandt, D. Schmeißer and P. Bogdanoff, *J. Mater. Chem. A*, 2014, **2**, 2663–2670.

26 C. H. Choi, C. Baldizzone, G. Polymeros, E. Pizzutilo, O. Kasian, A. K. Schuppert, N. Ranjbar Sahraie, M. T. Sougrati, K. J. J. Mayrhofer and F. Jaouen, *ACS Catal.*, 2016, **6**, 3136–3146.

27 M. T. Sougrati, V. Goellner, A. K. Schuppert, L. Stievano and F. Jaouen, *Catal. Today*, 2016, **262**, 110–120.

28 H. T. Chung, D. A. Cullen, D. Higgins, B. T. Sneed, E. F. Holby, K. L. More and P. Zelenay, *Science*, 2017, **357**(6350), 479–484.

29 Q. Jia, N. Ramaswamy, U. Tylus, K. Strickland, J. Li, A. Serov, K. Artyushkova, P. Atanassov, J. Anibal, C. Gumeci, S. Calabrese, M.-T. Sougrati, F. Jaouen, B. Halevi, S. Mukerjee, S. C. Barton, M.-T. Sougrati, F. Jaouen, B. Halevi, S. Mukerjee, S. Calabrese, M.-T. Sougrati, F. Jaouen, B. Halevi and S. Mukerjee, *Nano Energy*, 2016, **29**, 65–82.

30 U. Tylus, Q. Jia, K. Strickland, N. Ramaswamy, A. Serov, P. Atanassov and S. Mukerjee, *J. Phys. Chem. C*, 2014, **118**, 8999–9008.

31 Y. Chen, I. Matanovic, E. Weiler, P. Atanassov and K. Artyushkova, *ACS Appl. Energy Mater.*, 2018, **1**, 5948–5953.

32 H. Fei, J. Dong, Y. Feng, C. S. Allen, C. Wan, B. Volosskiy, M. Li, Z. Zhao, Y. Wang, H. Sun, P. An, W. Chen, Z. Guo, C. Lee, D. Chen, I. Shakir, M. Liu, T. Hu, Y. Li, A. I. Kirkland, X. Duan and Y. Huang, *Nat. Catal.*, 2018, **1**, 63–72.

33 J. Li, S. Ghoshal, W. Liang, M. T. Sougrati, F. Jaouen, B. Halevi, S. McKinney, G. McCool, C. Ma, X. Yuan, Z. F. Ma, S. Mukerjee and Q. Jia, *Energy Environ. Sci.*, 2016, **9**, 2418–2432.

34 U. I. Koslowski, I. Abs-Wurmbach, S. Fiechter and P. Bogdanoff, *J. Phys. Chem. C*, 2008, **112**, 15356–15366.

35 U. I. Kramm, I. Herrmann-Geppert, J. Behrends, K. Lips, S. Fiechter and P. Bogdanoff, *J. Am. Chem. Soc.*, 2016, **138**, 635–640.

36 N. D. Leonard, S. Wagner, F. Luo, J. Steinberg, W. Ju, N. Weidler, H. Wang, U. I. Kramm and P. Strasser, *ACS Catal.*, 2018, **8**, 1640–1647.

37 X. Li, K. Zhu, J. Pang, M. Tian, J. Liu, A. I. Rykov, M. Zheng, X. Wang, X. Zhu, Y. Huang, B. Liu, J. Wang, W. Yang and T. Zhang, *Appl. Catal., B*, 2018, **224**, 518–532.

38 Q. Jia, N. Ramaswamy, U. Tylus, K. Strickland, J. Li, A. Serov, K. Artyushkova, P. Atanassov, J. Anibal, C. Gumeci, S. Calabrese, M. Sougrati, F. Jaouen, B. Halevi and S. Mukerjee, *Nano Energy*, 2016, **29**, 65–82.

39 U. I. Kramm, L. Ni and S. Wagner, *Adv. Mater.*, 2019, **31**, 1805623.

40 F. A. Walker, *Coord. Chem. Rev.*, 1999, **185–186**, 471–534.

41 H. Schulenburg, S. Stankov, V. Schünemann, J. Radnik, I. Dorbandt, S. Fiechter, P. Bogdanoff and H. Tributsch, *J. Phys. Chem. B*, 2003, **107**, 9034–9041.

42 P. Gütlich, E. Bill and A. X. Trautwein, *Mössbauer Spectroscopy and Transition Metal Chemistry – Fundamentals and Applications*, Springer-Verlag Berlin Heidelberg, Heidelberg, 2011.

43 A. F. Holleman, N. Wiberg and E. Wiberg, *Lehrbuch der Anorganischen Chemie*, Walter de Gruyter & Co., Berlin, 102nd edn, 2008.

44 T. J. Schmidt, H. A. Gasteiger, G. D. Stäb, D. M. Kolb and R. J. Behm, *J. Electrochem. Soc.*, 1998, **145**, 2354–2358.

45 U. I. Kramm, I. Abs-Wurmbach, I. Herrmann-Geppert, J. Radnik, S. Fiechter and P. Bogdanoff, *J. Electrochem. Soc.*, 2011, **158**, B69–B78.

46 K. Ebner, J. Herranz, V. A. Saveleva, B. Kim, S. Henning, M. Demicheli, F. Krumeich, M. Nachtegaal and T. J. Schmidt, *ACS Appl. Energy Mater.*, 2019, **2**, 1469–1479.

47 F. Jaouen, J. Herranz, M. Lefevre, J. P. Dodelet, U. I. Kramm, I. Herrmann, P. Bogdanoff, J. Maruyama, T. Nagaoka, A. Garsuch, J. R. Dahn, T. Olson, S. Pylypenko, P. Atanassov and E. A. Ustinov, *ACS Appl. Mater. Interfaces*, 2009, **1**, 1623–1639.

48 A. H. Clark, P. Steiger, B. Bornmann, S. Hitz, R. Frahm, D. Ferri and M. Nachtegaal, *J. Synchrotron Radiat.*, 2020, **27**, 681–688.

9156 | *Phys. Chem. Chem. Phys.*, 2021, **23**, 9147–9157

This journal is © the Owner Societies 2021

49 O. Müller, M. Nachtegaal, J. Just, D. Lützenkirchen-Hecht and R. Frahm, *J. Synchrotron Radiat.*, 2016, **23**, 260–266.

50 B. Ravel and M. Newville, *J. Synchrotron Radiat.*, 2005, **12**, 537–541.

51 A. H. Clark, J. Imbao, R. Frahm and M. Nachtegaal, *J. Synchrotron Radiat.*, 2020, **27**, 551–557.

52 S. J. Archibald, S. L. Atkin, W. Bras, A. Diego-Taboada, G. Mackenzie, J. F. W. Mosselmans, S. Nikitenko, P. D. Quinn, M. F. Thomas and N. A. Young, *J. Mater. Chem. B*, 2014, **2**, 945–959.

53 Y. Hu, J. O. Jensen, W. Zhang, L. N. Cleemann, W. Xing, N. J. Bjerrum and Q. Li, *Angew. Chem., Int. Ed.*, 2014, **53**, 3675–3679.

54 D. Deng, L. Yu, X. Chen, G. Wang, L. Jin, X. Pan, J. Deng, G. Sun and X. Bao, *Angew. Chem.*, 2013, 389–393.

55 Z. Wen, S. Ci, F. Zhang, X. Feng, S. Cui, S. Mao, S. Luo, Z. He and J. Chen, *Adv. Mater.*, 2012, **24**, 1399–1404.

56 J. P. Dodelet, R. Chenitz, L. Yang and M. Lefèvre, *ChemCatChem*, 2014, **6**, 1866–1867.

57 D. Y. Chung, S. W. Jun, G. Yoon, S. G. Kwon, D. Y. Shin, P. Seo, J. M. Yoo, H. Shin, Y.-H. Chung, H. Kim, B. S. Mun, K.-S. Lee, N.-S. Lee, S. J. Yoo, D.-H. Lim, K. Kang, Y.-E. Sung and T. Hyeon, *J. Am. Chem. Soc.*, 2015, **137**, 15478–15485.

58 F. Tuinstra and J. L. Koenig, *J. Chem. Phys.*, 1970, **53**, 1126–1130.

59 A. C. Ferrari, J. C. Meyer, V. Scardaci, C. Casiraghi, M. Lazzeri, F. Mauri, S. Piscanec, D. Jiang, K. S. Novoselov, S. Roth and A. K. Geim, *Phys. Rev. Lett.*, 2006, **97**, 187401.

60 I. Herrmann, U. I. Kramm, J. Radnik, S. Fiechter and P. Bogdanoff, *J. Electrochem. Soc.*, 2009, **156**, B1283–B1292.

61 A. Sadezky, H. Muckenhuber, H. Grothe, R. Niessner and U. Pöschl, *Carbon*, 2005, **43**, 1731–1742.

62 A. C. Ferrari and J. Robertson, *Phys. Rev. B: Condens. Matter Mater. Phys.*, 2000, **61**, 95–107.

63 G. Wu and P. Zelenay, *Acc. Chem. Res.*, 2013, **46**, 1878–1889.

64 M. Yudasaka and R. Kikuchi, in *Supercarbon – Synthesis, Properties and Applications*, ed. S. Yoshimura and R. P. H. Chang, Springer-Verlag Berlin Heidelberg GmbH, Heidelberg, 1998, pp. 99–105.

65 H. Marsh and A. P. Warburton, *J. Appl. Chem.*, 1970, **20**, 133–142.

66 S. Wagner, H. Auerbach, C. E. Tait, I. Martinaiou, S. C. N. Kumar, C. Kübel, I. Sergeev, H.-C. Wille, J. Behrends, J. A. Wolny, V. Schünemann and U. Kramm, *Angew. Chem., Int. Ed.*, 2019, **58**, 10486–10492.

67 M. Newville, XAFS Spectra Library, http://cars.uchicago.edu/xaslib/spectrum/729, accessed 8 June 2017.

68 I. Matanovic, K. Artyushkova and P. Atanassov, *Curr. Opin. Electrochem.*, 2018, **9**, 137–144.

69 I. H. M. van Stokkum, K. M. Mullen and V. V. Mihaleva, *Chemom. Intell. Lab. Syst.*, 2009, **95**, 150–163.

70 C. Ruckebusch and L. Blanchet, *Anal. Chim. Acta*, 2013, **765**, 28–36.

71 A. Voronov, A. Urakawa, W. van Beek, N. E. Tsakoumis, H. Emerich and M. Rønning, *Anal. Chim. Acta*, 2014, **840**, 20–27.

72 F. Jaouen, M. Lefèvre, J.-P. Dodelet and M. Cai, *J. Phys. Chem. B*, 2006, **110**, 5553–5558.

73 K. Artyushkova, A. Serov, S. Rojas-Carbonell and P. Atanassov, *J. Phys. Chem. C*, 2015, **119**, 25917–25928.

74 U. I. Kramm, M. Lefèvre, N. Larouche, D. Schmeisser and J.-P. Dodelet, *J. Am. Chem. Soc.*, 2014, **136**, 978–985.

75 C. E. Szakacs, M. Lefevre, U. I. Kramm, J.-P. P. Dodelet and F. Vidal, *Phys. Chem. Chem. Phys.*, 2014, **16**, 13654–13661.

76 Q. Jia, N. Ramaswamy, H. Hafiz, U. Tylus, K. Strickland, G. Wu, B. Barbiellini, A. Bansil, E. F. Holby, P. Zelenay and S. Mukerjee, *ACS Nano*, 2015, **9**, 12496–12505.

77 M. Primbs, Y. Sun, A. Roy, D. Malko, A. Mehmood, M.-T. Sougrati, P.-Y. Blanchard, G. Granozzi, T. Kosmala, G. Daniel, P. Atanassov, J. Sharman, C. Durante, A. Kucernak, D. Jones, F. Jaouen and P. Strasser, *Energy Environ. Sci.*, 2020, **13**, 2480–2500.